Since January 2020 Elsevier has created a COVID-19 resource centre with free information in English and Mandarin on the novel coronavirus COVID-19. The COVID-19 resource centre is hosted on Elsevier Connect, the company's public news and information website.

Sensing and Bio-Sensing Research 37 (2022) 100510

Contents lists available at ScienceDirect

Sensing and Bio-Sensing Research

journal homepage: www.elsevier.com/locate/sbsr

Piezoelectric point-of-care biosensor for the detection of SARS-COV-2 (COVID-19) antibodies

Debdyuti Mandal, Mustahseen M. Indaleeb, Alexandra Younan, Sourav Banerjee *

Integrated Material Assessment and Predictive Simulation Laboratory, University of South Carolina, Columbia, SC, USA

ARTICLE INFO

Keywords:
Piezoelectric biosensor
Surface acoustic waves
SAW
POC biosensor
Covid-19
SARS

ABSTRACT

It is always challenging to diagnose a disease using a biosensor reliably, and quickly with high sensitivity and selectivity, simultaneosuly. Recently the world experienced a global pandemic caused by a novel coronavirus (COVID-19). Although the vaccines are available, COVID-19 resulted a huge threat to the entire world with high mortality rates. Irrespective of a specific disease, there is a constant need for a cheaper and faster in-vitro, lab-on-a-chip sensor with high sensitivity and selectivity. Such sensors will not only facilitate the disease detection but will expedite and vaccine development process through detection of its corresponding antibodies when developed. In this article, we present an ultrasonic guided wave sensor using 128° YX lithium niobate piezoelectric wafer, specially designed in a shape of a multi-threaded comb with cantilever beams which is equally selective and sensitive for the detection of corresponding antigen-antibody assays. As a proof of concept in this article, the diagnostic sensor is created and tested for detection of SARS-COV-2 antibodies. Sensors were functionalized with SARS-COV-2 antigens and target antibody for the same was detected. Unique and judicially tuned acoustic features are analyzed for successful detection of the right antibodies. The proposed lab-on-a-chip device utilizes a wide range of diagnostic frequencies resulting into a highly sensitive platform for the diagnostics even to the slightest biophysical changes. The proposed sensor is also believed to extend to the detection of various other antigens/antibodies of different diseases in the future.

1. Introduction

In December 2019, atypical respiratory disease outbroke was first reported in Wuhan, China. It was then discovered that the novel coronavirus was responsible for that event. Severe acute respiratory syndrome coronavirus-2 (SARS-COV-2) resulted acute respiratory distress syndrome and caused high mortality rates. The virus transmitted rapidly throughout the world. Eventually, the World Health Organization (WHO 2020) classified and declared coronavirus disease (COVID-19) outbreak as a global pandemic. As of January 2022, around 351 million cases are reported worldwide and around 5.6 million people died of COVID-19. approximately 72 million cases are reported in the United States with a mortality of around 890,000 [1]. At present, vaccines are available, and people all around the world are getting vaccinated. Unfortunately, the vaccines were not available during 2019–2020, which was devastating. The vaccine development process usually takes place in three ways, namely, live vaccines, inactivated vaccines, and genetically engineered vaccines [2]. Maintaining proper clinical guidelines and followed by the trials in animals usually takes up to 3–6 months of time. Covering these steps and ensuring quality and safety, the clinical trials are moved to the testing on humans which then goes through 3–4 phases and takes about 12–18 months before proper approval. Therefore, in such cases of a pandemic outbreak, while vaccines are still getting developed, a huge number of easy-to-use and fast diagnostic devices are required. Biosensors are needed to detect the disease in the early stages. They could also help discover and testing the potential antibodies for vaccine development.

Since the COVID-19 outbreak, there are many available methods for diagnostics. Chest CT is one of the viable methods, however, used for temporary diagnostic only. It involves the imaging of different cross-sections of the chest using X-rays at different angles which often is used in determining COVID-19 pneumonia and determining the extent of lung infection [3]. Loop mediated isothermal amplification (LAMP) is another detection technique used for the diagnostic process where the technique is similar to RT-PCR, the specific DNA sequences of the viruses are amplified [3]. Serological tests are another common method utilized for the detection of COVID-19. Although these methods are effective, they have disadvantages like, being highly expensive, low reusability

* Corresponding author.
E-mail address: banerjes@cec.sc.edu (S. Banerjee).

https://doi.org/10.1016/j.sbsr.2022.100510
Received 13 April 2022; Received in revised form 29 June 2022; Accepted 12 July 2022
Available online 14 July 2022

and require highly trained staffs [3]. The microarray method was also investigated during the COVID-19 outbreak which involves the hybridization of the mRNA molecule to DNA template from the origin. Electrochemical sensors are also widely utilized for virus detection. Recent studies shows that different electrochemical techniques such as conductometry, amperometry, cyclic voltammetry, EIS, potentiometry, and chrono-amperometry are useful for successful diagnostics [4]. Electrochemical techniques are very promising in the field of diagnostics especially due to their benefits of high sensitivity, rapid analysis, and lost cost equipment, but it also has certain drawbacks. Drawbacks such as electrode fouling, issues related to analyte mass transport or diffusion, error in current-potential, issues related to counter electrodes, etc. reduce the limit of detection, quantification [5]. Additionally, nanotechnology-based methods such as the utilization of nanospheres, quantum dots, nanotubes, metal oxide nanorods, etc. are integrated with the sensors for higher sensitivity leading to better diagnostics [6]. Altogether, the modern field of biosensing involves various sensing techniques such as optical, electrochemical, magnetic, thermometric-based techniques, etc. [7–10]. Many of such approaches require very intensive and complicated setups which are not easy to access and sometimes are not user-friendly. For example, reverse transcription-polymerase chain reaction (RT-PCR) is a conventional method [11] for diagnosing the COVID-19 virus, but this method is still not rapidly available and affordable in many countries. The RT-PCR requires a laboratory, a couple of chemical reagents, and skilled personnel to perform the tests. These sensing techniques struggle in terms of developing simple, portable, and inexpensive setups and models. These techniques cost time and labor. At times mal-handlings lead to false-positives and false-negatives. Few other techniques like optical-based sensing consist of equipment that require periodic rinsing to prevent biofouling. They are also limited to being used in the laboratories because the fluorescent detection instrumentation is too bulky, and lacking portability for point-of-care use. Therefore, to overcome such issues, there is an essential need for a Point-Of-Care (POC) sensing mechanism on a biosensing platform, which is portable, in-vitro, and provides real-time analysis at the onsite screening of the samples. The piezoelectric sensing is observed effectively. These methods drastically reduce the costs for the sensing setup and enhance the precision, by providing in-vitro real-time analysis [12–14]. Additional benefits like high sensitivity, the flexibility of sensor size and low power consumption, and better sensitivity even at the low scale of the biomarker concentrations [15–17] are evident. *Kabir* et al. (2021) utilized a PVDF-based piezoelectric microcantilever that is highly sensitive to mass-inducing stress, leading to tip deflections [18]. *Zuo* et al. (2004) investigated the piezoelectric-based sensing of SARS-COV on an oscillating AT-cut PZ crystal sensitive to mass. Thus, frequency shifts were induced due to mass and were sensed up to a detection limit of 0.6 mg/ml [19]. *Kim* et al. (2015) introduced a piezoresistive microcantilever integrated with magnetic nanobeads for the detection of HPV genotype. The magnetic force in the cross-sectional direction compelled the magnetic beads associated with the biocomplex to deflect and sense [20]. Similarly, *Wee* et al. (2005) developed a novel electrical detection of prostate-specific antigens and C-reactive proteins using piezoresistive self-sensing micro-cantilevers. The system included piezoresistive cantilevers along with the immobilization of the biosensitive layer and detection of antigens using the fundamental of mass-induced deflection [21]. The piezoelectric biosensors have the advantage of rapid results, highly specific, label-free, and highly sensitive features. In the conventional detection process, a biocomplex results in the addition of mass that usually decreases the frequency controlled by the AC voltage [22,23].

In this article, we present a coupled ultrasonic Guided wave sensor using a 128° YX lithium niobate piezoelectric wafer, specially designed in a shape of a multi-threaded comb with cantilever beams which is equally selective and sensitive for the detection of target antigen-antibody assays. As a proof of concept in this article, the diagnostic sensor is created and tested for the detection of SARS-COV-2 antibodies. The presented concept will as well work for diagnostics of other pathogen-based diseases. Objective of this article to present the possibility of detection of SARS-COV-2 antibodies using a new physics of Guided wave. The proposed physics has not been tried before. Hence, absolute detection and frequency of activations are emphasized in this article over the limit of detection. The unique sensing method relies on the effective design of the piezoelectric cantilever beams of varying lengths made of lithium niobate crystal. Ultrasonic guided wave-based sensing using cantilever configuration was achieved for the first time. Conventional surface acoustic wave (SAW) sensors are used using the physics of Guided waves. However, multiple detection in a same platform is not possible. *It is proposed that if a platform can self-confirm the detection with multiple detection spots (like multiple sensors in a same platform), desired sensitivity and selectivity through cross verification of the detection in single device is achievable and desirable.* In this proposed method, Guided wave ultrasound is used but was exploited at multiple detection ports creating array of cantilever beams of varying lengths (thus creates different nature of sensors due to variable frequency response). Please note that here the conventional bending of the cantilever beams are not the physics used for detection, but the Guided wave propagated in each beam element at a modal frequency is used for the detection. Medium frequency range 1 MHz- 5 MHz is specifically targeted to employ small hardware that can be connected to the sensor in the future. In this work, a series of piezoelectric cantilever beams of varying lengths are chemically coated and functionalized to form a test bed/baseline of the spike proteins. The chosen cantilever beam is excited with a unique tone burst signal that results in generations of ultrasonic signals which then interact with the other geometrically varied cantilever beams with different guided frequency identity. The sensor is treated with the appropriate SARS-COV-2 antibodies and as a result of the diagnostic step, the piezoelectric response is monitored. Different acoustic feature extraction techniques such as Fast Fourier Transform (FFT), Power Spectrum Density (PSD), and Spectrogram, were used for the validation of the detection. Data were analyzed for confirming the antigens-antibodies binding affinity by virtue of the piezoelectric signals (collected from all beams). The proposed sensing platform is highly sensitive to even the slightest change of specific micro-nanograms and is believed to be actively operational in the case of diagnosing the COVID -19 virus (inverse diagnosis of the proposed ones). One sensor having 10 cantilever beam is essentially 10 sensors in a same platform mutually confirming the detection. Other diseases could also be diagnosed if the piezo substrate is functionalized accordingly. The proposed method will be a rapid solution to early diagnostics and for discovering potential antibodies during an outbreak of diseases in the future.

2. Materials and methods

2.1. Chemicals and reagents

The Recombinant SARS-CoV-2 Spike Protein and the Polyclonal Rabbit antibody against SARS-CoV-2 (COVID-19) Spike Protein Subunit 2 (S2F) Protein were purchased from *RayBiotech. N-(3-Dimethylaminopropyl)-N′-ethylcarbodiimide hydrochloride* (EDC), *N-Hydroxysuccinimide* (NHS), *Ethanolamine, Thiourea, Phosphate Buffer Saline* (PBS) and *DI water* were purchased from *Sigma Aldrich*. The Polyethylene Glycated (PEG) functionalized 10 nm Biopure Gold nanospheres were purchased from *NanoComposix*. 128° YX- cut Lithium Niobate Piezoelectric wafers of 350 μm thickness were purchased from *Custom Glass and Optics*, USA.

2.2. Fabrication of the Lithium Niobate cantilevers

The Lithium niobate cantilevers were fabricated using metal deposition and laser cutting processes. The wafers were deposited with Titanium and Gold layers on both sides of the Lithium niobate wafer. The deposition process was performed using the *Denton E-Beam Evaporator*

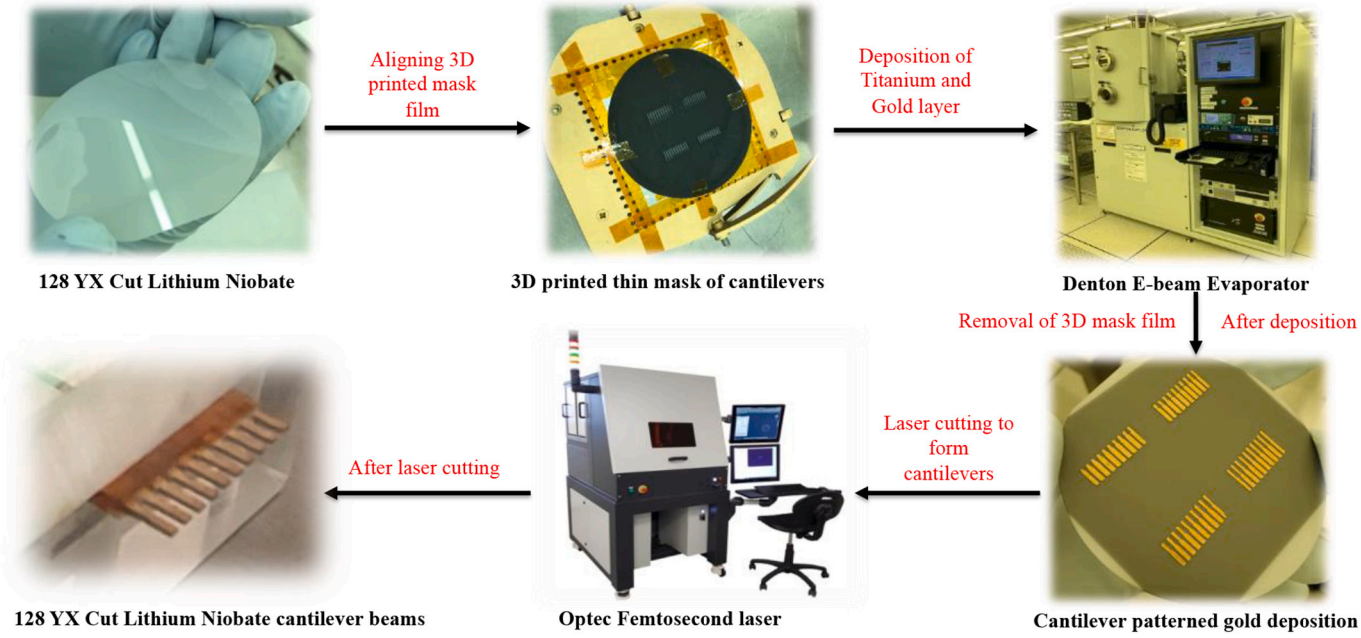

Fig. 1. Fabrication process of the gold coated lithium niobate piezoelectric cantilever beams. (For interpretation of the references to colour in this figure legend, the reader is referred to the web version of this article.)

System from the *Institute for Electronics and Nanotechnology (IEN) at Georgia Institute of Technology*. Approximately 100 nm thick Titanium layer followed by 2 μm of the gold layer were deposited at the rate of 1 Å/s deposition rate and at a pressure of 5e-006 (Pa). The purpose of the Titanium layer is for the better adhesion of the gold layer to the substrate. The gold layer was used for better conductivity and to support as a base to conjugate the bio and nano-functionalized layers on top of the wafer. The metal deposited piezoelectric wafer was cut using *the Optec Femtosecond Laser Micro-Machining* system which utilizes ultra-short laser pulses for the photo-based ablation. The wafer was cut into a chip-sized having 10 cantilevers at a progressive length with the longest beam of 5 mm length and the shortest beam of 4.1 mm with a progression of 0.1 mm length for each successive beam. The gap between all the beams along with their width was constant to a length of 1 mm. One of the sides of the chip was then laser engraved to electrically isolate all the individual beams coated with gold and the other flip side was left as it is for the electrical grounding purpose. Fig. 1 shows the fabrication process of the gold-coated piezoelectric cantilever beams. The beams were electrically connected using thin conductive copper strips. Further, they were covered and insulated using the Kapton tapes.

2.3. Surface functionalization of the Lithium Niobate cantilevers

The lithium niobate wafers were washed multiple times using ethanol and DI water and dried with nitrogen gas before the functionalization process. The gold cantilever beams were coated with a *Self-Assembled Monolayer (SAM)* by the addition of 100 mM of Thiourea solution in DI water overnight. The cantilever beams were then rinsed with ethanol and DI water to remove the excess thiourea from the sample. The second step of the functionalization process was the addition of the gold nanoparticles layer on top of the SAM-coated cantilever beams. In this process, the carboxylic encapsulated gold nanoparticles having 10 nm diameter were added on top of the SAM-coated cantilevers and were incubated for 10–12 h. The purpose of this step was to enhance the sensitivity of the sensing platform. The nanoparticles not only provide a better electron transfer rate and enhanced orientational freedom, but also a high surface-to-volume ratio that enables the feature of immobilizing more functionalized antibodies and subsequently more target antigens/antibodies based on the user's final target analyte [24–26]. This phenomenon results in a substantial increment in the probability of capturing the 'capture antibodies' even at very low

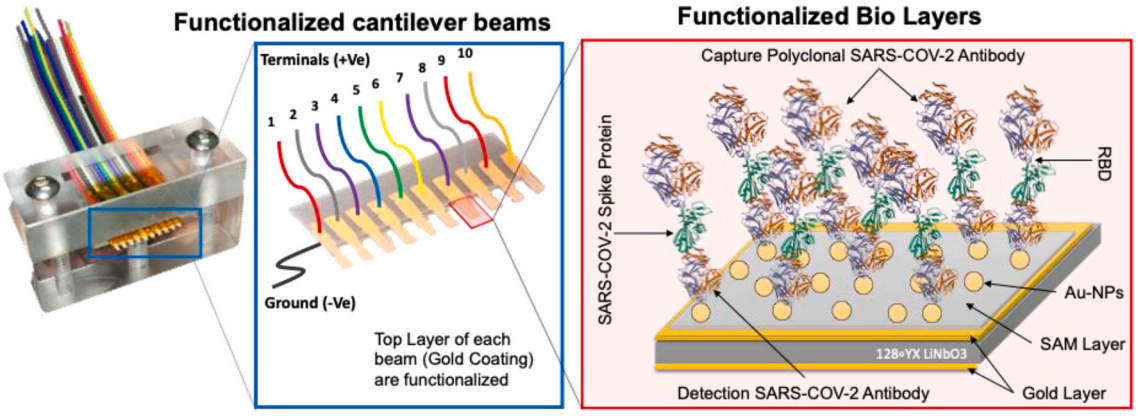

Fig. 2. Schematic of the functionalization layers on top of the gold coated lithium niobate piezoelectric cantilever beams. (For interpretation of the references to colour in this figure legend, the reader is referred to the web version of this article.)

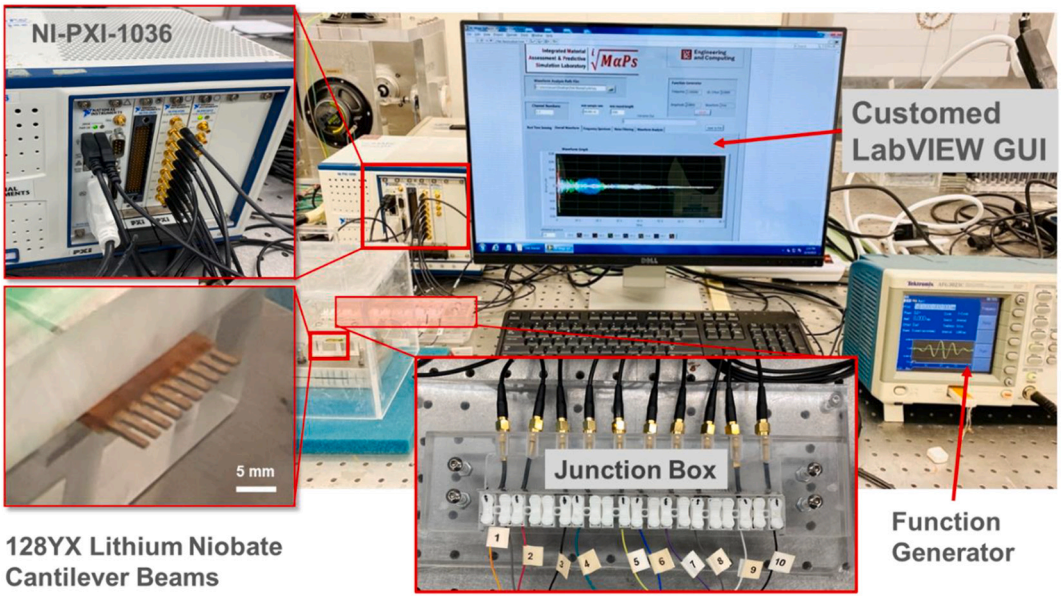

Fig. 3. Collage showing the of the experimental setup with its respective components.

concentrations that contribute to better sensitivity. Completing the incubation process, the nanoparticles were surface activated by the addition of 75 mM N-*(3-Dimethylaminopropyl)-N′-ethylcarbodiimide hydrochloride* (EDC) and followed by 50 mM *N-Hydroxysuccinimide* (NHS) for the covalent binding of the detection antibodies to the gold nanoparticles.

2.4. Immobilization of the SARS-CoV-2 spike protein

The gold nanoparticles coated cantilever sensor was rinsed using PBS (pH 7.4) and dried with nitrogen gas to remove the excess nanoparticles. In the next step, 5 μl of 0.5 mg/ml Rabbit anti-SARS-CoV-2 S2F antibodies (*detection antibodies*) were added to the surface-activated cantilevers and incubated for 4 h at 4 °C. The sensor was rinsed with PBS and then added with 5 μl of Recombinant SARS-CoV-2 Spike Protein, S2 Subunit, and incubated for 6–8 h at 4 °C. In the next step, the non-reacted sensor surface was blocked by adding 1 μl of ethanolamine on top of the cantilever's sensor. This is the 'baseline' of the lithium niobate cantilever-based sensing on which different antibodies are to be tested.

2.5. Addition of the SARS-CoV-2 capture antibodies

The cantilevers sensor was tested for the SARS-CoV-2 capture antibodies. The sensor surface was rinsed with PBS and in the final step, the acoustic readings were captured before and after adding 5 μl of 0.5 mg/ml concentration of the SARS-CoV-2 *capture* antibodies to the sensor surface. Fig. 2 represents the schematic of the functionalized layers on top of the cantilever beams.

3. Instrumentation and acoustic measurements

All acoustic measurements were carried out using NI-PXI-1036 (NI) system. The NI system is equipped with NI PXI-5412, 100 MS/s Arbitrary Waveform Generator, 14-bit, 8 MB, NI PXI-5105, 8-ch, 60 MS/s Digitizer w/16 MB Onboard Memory, NI PXI-2570 40 Channel Form C Relay Module, Windows 7 32-Bit For NI PXI Embedded Controllers, NI PXI-8102 Celeron T3100 1.9 GHz Controller. The NI system uses a custom-developed integrated LabView software for the data acquisition and as a result, a Graphical User Interface (GUI) was designed and developed for easy and quick measurements of the ultrasound signals. An electrical junction box having 10 channels was also fabricated where the subminiature version B (SMB) type connectors were connected to the NI system. Fig. 3 demonstrates the schematic diagram of the circuit along with the actual setup. The experiments were carried out in 3 stages.

Stage 1: After the beams were functionalized without placing the SARS-COV-2 antigens 'baseline', a pristine set of data was collected in which a particular beam was excited and all the other respective 9 beams were used as sensors. A *5-count tone burst* signal with a single cycle was triggered throughout the experiments with the frequency ranging from 700 kHz to 5.5 MHz at an interval of 200 kHz at each measurement. It was observed that the signal responses were not significant and were below noise level for the case of the first (beam 1) terminal and the last terminal (beam 10) possibly due to manufacturing defects. Hence, they were omitted from all the following experiments and analyses. In the latter stages, cantilever beam number 6 was marked as an exciter and all the other beams (aforementioned, except 1 and 10) as sensors.

Stage 2: Next the beams were functionalized with SARS-COV-2 antigens 'baseline'. Following the similar schedule discussed above, the second set of 'baseline' data were collected to measure and quantify the effect of the addition of antigens on the functionalized layer.

Stage 3: Finally SARS-COV-2 capture antibodies were added on top of the 'baseline' beam arrays. Again, a similar schedule of data sets was collected from each beam except for beams 1 and 10.

Please note that for all experiments, beam 6 (terminal 6) was not coated with any of the bio/chemical layers. All the acoustic measurements were carried out at a sample rate of 40 MS/s and 3000 data points were collected for each measurement. Each set of experiments was repeated three times and all data were curated. Please note that terminal no. and beam no. are synonymously used hereafter.

4. Results and discussion

Please note that the results presented in the following section are for the understanding the system and used for the development of the software for data analysis in real-time. In-vitro diagnostics of a disease using the proposed sensor would not require the following extended process but will require excitation of a specific frequency found through the study reported in the following section followed by a quick analysis present in the sensor chip.

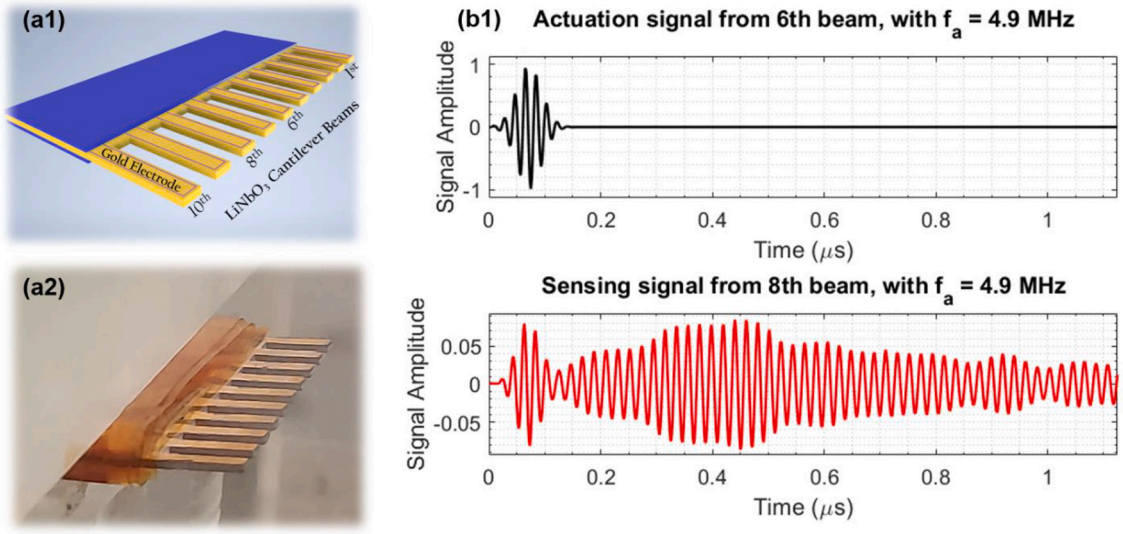

Fig. 4. (a1) Schematic of the cantilever beams, (a2) actual cantilever beams, (b1) 5- count tone burst signal and (b2) signal response from the sensing beam 4.

4.1. *Tone burst signal: excitation and sensing*

In this section, the fundamental process of the excitation and the sensing mechanisms using the 5-count tone burst signal is described. The tone burst signal was generated using a simple sinusoidal wave coupled with the Hanning window function. Eq. (1) describes the generic equation for the tone burst signal used for the signal excitation.

$$X(t) = sin(2\pi ft) * e^{-p*\frac{(t-T0)^2}{2}};\ T0 = T\Big/2;\ T = N\Big/f \tag{1}$$

Where, N is the number of cycles, f is the central frequency, t is the time and T0 refers to the time-period of the burst signal, and p is a

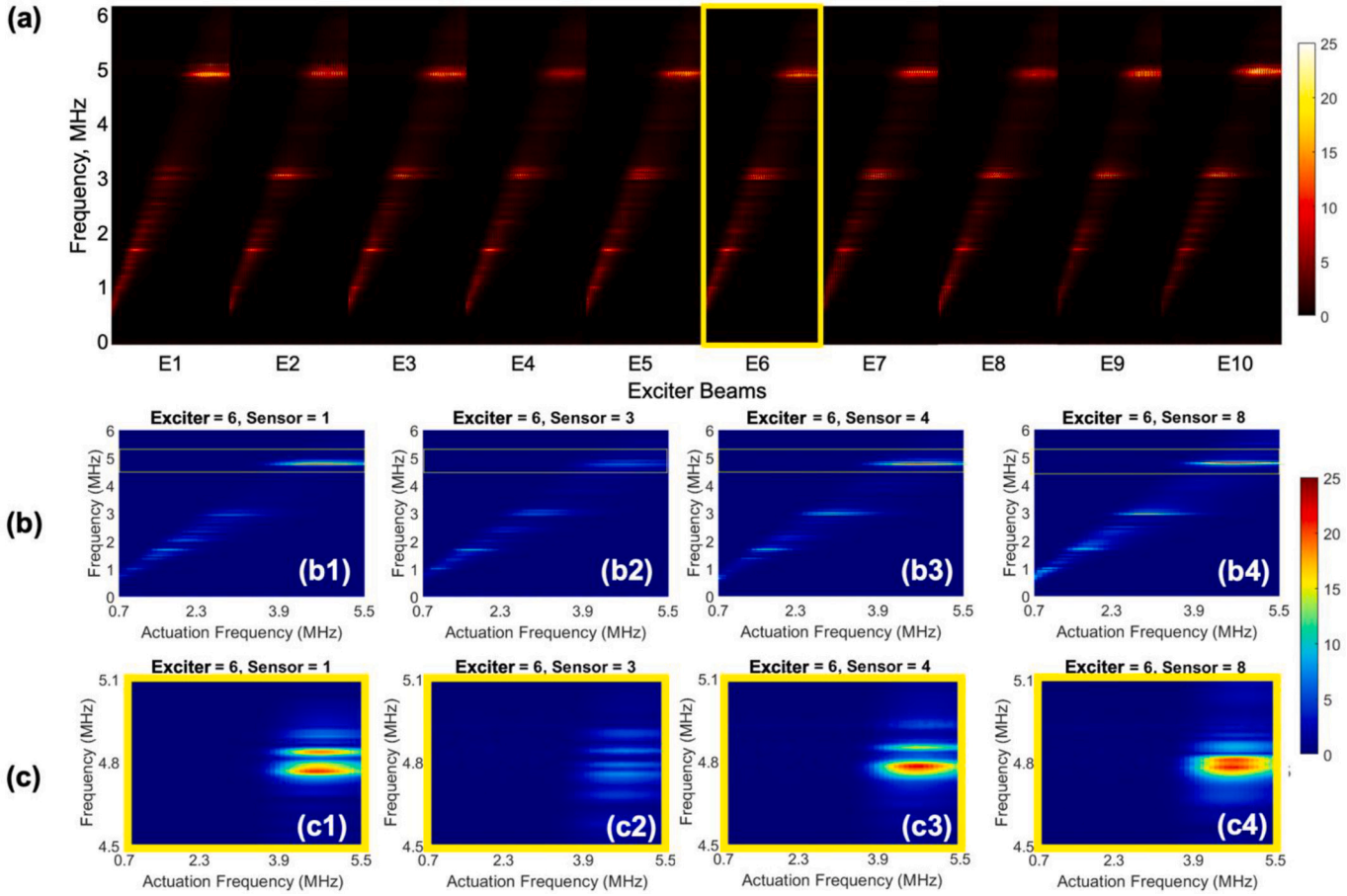

Fig. 5. (a) FFT heat map of all the cantilever beams (pristine), (b) FFT spectral analysis of sensor beams 1,3,4,8. (c) zoomed FFT spectrum at 4.9 MHz excitation frequency.

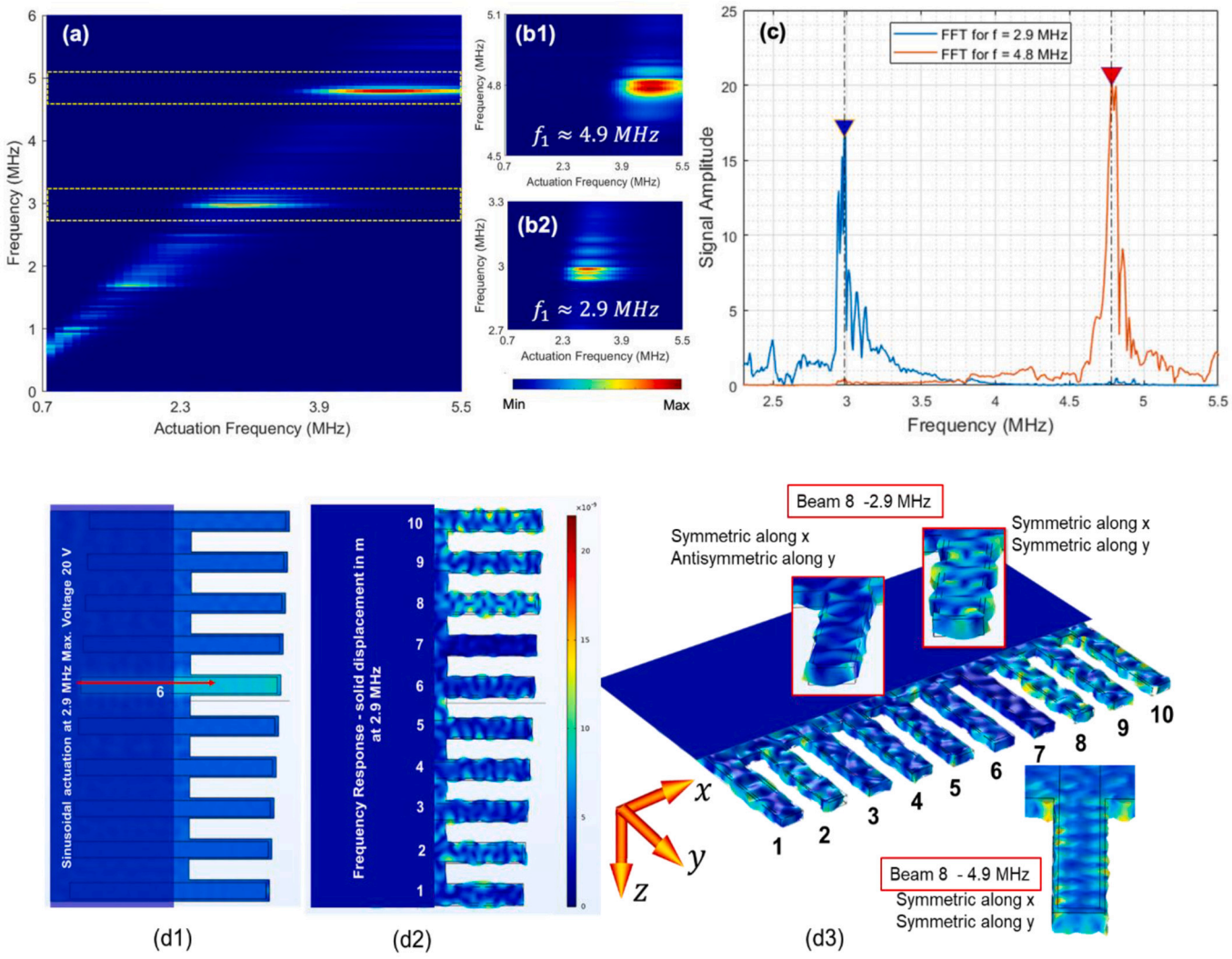

Fig. 6. (a) FFT spectral map of sensing beam 8, (b1) zoomed FFT spectral map at 4.9 MHz, (b2) zoomed FFT spectral map at 2.9 MHz (c) 2D-FFT plot of sensing beam 8 at 4.9 MHz and 2.9 MHz excitation frequency, (d1) frequency domain simulation, actuation of 6th beam, (d2) top view (x-y plane) of the total solid displacement field in each beam, and (d3) 3D view of the total sold displacement field for each beam with an inset showing zoom views of the displacement field for beam 5 and beam 8 (both at 2.9 Mhz and 4.9 MHz).

shapefactor defined as (5**f*)/*N* This type of signal is widely used in the field of structural health monitoring for non-destructive evaluation methods. The excited tone burst signal is electrically transmitted through the input terminal (e.g. terminal associated with beam 6). Through electromechanical transduction, the input electrical energy is converted to mechanical stresses, and the stress wave propagated through the specimen in form of wave packets. These wave packets then interact with the complete geometry of a specimen and individual beams responded with their unique vibration signature. The mechanical wave feature then through mechanoelectrical transduction process is converted to an electrical signal which is captured by the NI system. Different beams act like different sensors and then capture the signal response. The signal captured by NI was then analyzed using multiple acoustic feature extraction tools custom programmed in MATLAB for the quantification of detection. The study explains the properties and its characterization of the specimen. In this experiment, being at the center, beam number 6 was excited throughout with the tone burst signal. As the substrate is a piezoelectric material made of 128° YX cut Lithium Niobate, it generated guided waves that propagated inside the wafer (sensor body and all the beams) that were laser cut to create unique beam geometries. The experiments were repeated with different input central frequency *f* ranges between 700 kHz – 5 MHz at an interval of 200 kHz. The piezoelectric responses were captured and monitored from different sensing beams corresponding to each different excitation frequencies.

Fig. 4 shows a schematic of the 5-count tone burst signal excited at the frequency at 700 kHz given to beam 6 and the sensing response from the beam 4. As it can be seen, that in addition to a crosstalk, multiple new wave packets are generated through wave dispersion. By virtue of different lengths, and distances from the actuator different beams demonstrate different dispersive responses. These dispersed waveforms carry important information based on the modal activation of the sensory beams. Such information is further decoded by different acoustic feature extraction methods to prove the functionality of the proposed biosensor.

4.2. *Excitation of the cantilever beam with the tone burst signal*

First, an input Burst signal was provided to the terminal associated with a specific cantilever beam one at a time, marked as an actuator or exciter (E). Wave signals were collected from the terminals associated with respective beams. As mentioned, signals were collected at different excitation frequencies, 700 kHz – 5.5 MHz at an interval of 200 kHz resulting in 49 frequencies. For each beam as an exciter, 49 sets of data

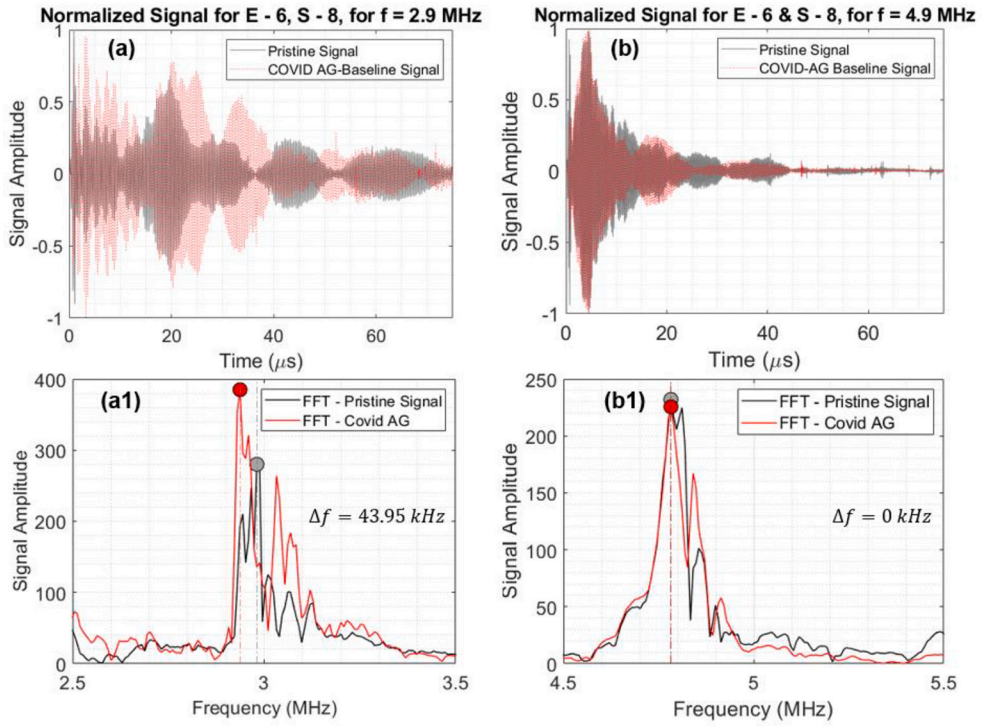

Fig. 7. Superimposed signal comparison of pristine and covid antigen baseline of sensing beam 8 at (a) 2.9 MHz and (b) 4.9 MHz. (a1) FFT of pristine vs. antigens and frequency shifts at 2.9 MHz. (b1) FFT of pristine vs. antigens and frequency shifts at 4.9 MHz.

were collected from 9 beams marked as the sensor. Thus, when an *i*-th beam was used as an actuator total of 49 × 9 = 401 wave signals were collected from one set of experiments automatically. This was repeated 3 times This way 10 × 3 = 30 sets of signals were collected to perform the analysis, where 10 represents the total number of beams in the wafer used as exciter (E). E*i* in Fig. 5(a) shows the i-th beam used as an actuator when *i* take values between 1 and 10. Fig. 5(a) shows the heat map of the average frequency contents of the acquired sensor signals plotted as an augmented surface frequency spectrum using Fast Fourier Transform (FFT). Here 49 × 9 = 401 FFT signals are augmented side by side for each beam as exciter. A general trend has emerged from the plot. It shows that significantly higher frequency response is obtained near ~4.9 MHz and ~ 2.9 MHz. It was also observed that when the 6th beam was an exciter the response signals from the other beams were promising with comparatively higher amplitude. Hence, 6th beam was chosen as an exciter to perform all the subsequent experiments and analysis reported herein.

Next, FFT of the signals collected from beam 1, beam 3, beam 4, and beam 8 is shown in Fig. 5 (b) over the range of 700 kHz to 5.5 MHz excitation frequencies. A frequency range around the ~4.9 MHz was found to provide the peak responses from all the beams that were used as sensors. Fig. 5 (c) shows the zoomed FFT spectrum in the frequency range between 4.5 and 5.1 MHz. Higher amplitudes are detected with multiple acoustic frequency lobes in this range for all the sensors. The spectral analysis of the signals collected from beam 8 (arbitrarily chosen) shows that there are multiple spectral peaks present in the frequency range. Major spectral peaks were observed around 800 kHz-1.2 MHz, 1.8 MHz, 2.9 MHz, and 4.9 MHz. Fig. 6 shows the FFT spectral map of beam 8 as a sensor.

Notably, 2.9 MHz and 4.9 MHz frequency ranges showed the highest amplitudes. Further to verify, 2D FFT plots are presented in Fig. 5(b1) and (b2). Fig, 5(c) shows that both the frequency ranges have a comparable signal amplitude of approximately 17 mV and 20 mV, respectively. It is evident that beam 8 has a maximum resonance at those frequencies. To verify this a COMSOL Multiphysics simulation (a Finite Element Analysis package, commercially available) was performed with exact geometry, material, and boundary conditions (please refer to document M1: Model detail, separately submitted with this document). Fig. 6 (d1) (d2) and (d3) show the frequency domain simulation result at 2.9 MHz only (4.9 MHz not shown however, simulations at all frequencies between 700 kHz – 5.5 MHz at an interval of 200 kHz were performed). Fig. 6(d1) shows the input electric potential and actuation voltage of 20 V with sinusoidal actuation frequency 2.9 MHz that was applied to the 6th terminal. Fig. 6(d2) shows the top view (x-y plane) of the total solid displacement field in each beam. Fig. 6(d3) shows the 3D view of the total sold displacement field for each beam with an inset showing zoom views of the displacement field for beam 5 and beam 8. Beam 8 has both symmetric wave modes along with x and y directions, whereas beam 5 has symmetric propagating modes along the x axis and antisymmetric wave mode along the y-axis. Precisely this was the reason for implementing multiple beams with multiple lengths to exploit two different wave modes in two orthogonal directions such that the responses could be non-identical for each beam and selectivity could be enhanced. Similar but higher frequency wave modes in the beams are evident at 4.9 MHz. It is understood that a wide range of frequencies could be accessed by different beams for sensing purposes. Users may have the freedom to experiment on a single beam or on multiple beams at a wide range of frequencies to cross-verify the sensitivity and selectivity.

4.3. *Signal analysis of the SARS-COV-2 antigen baseline*

Further signal analyses were performed with all the beams coated with the 'baseline' COVID-19 antigens (Stage 2) and were compared with the pristine state results (Stage 1). Although all the beams were tested, beam 8 is presented herein as the sensor because of its strong response and higher sensitivity at the actuation signal frequencies. Fig. 7 shows the frequency spectrum of the signals acquired from the pristine state and when the antigens were coated (we call antigen 'baseline' case). Maximum amplitudes are observed near 2.9 MHz and 4.9 MHz as identified above.

Although the further study was conducted at both frequency peaks

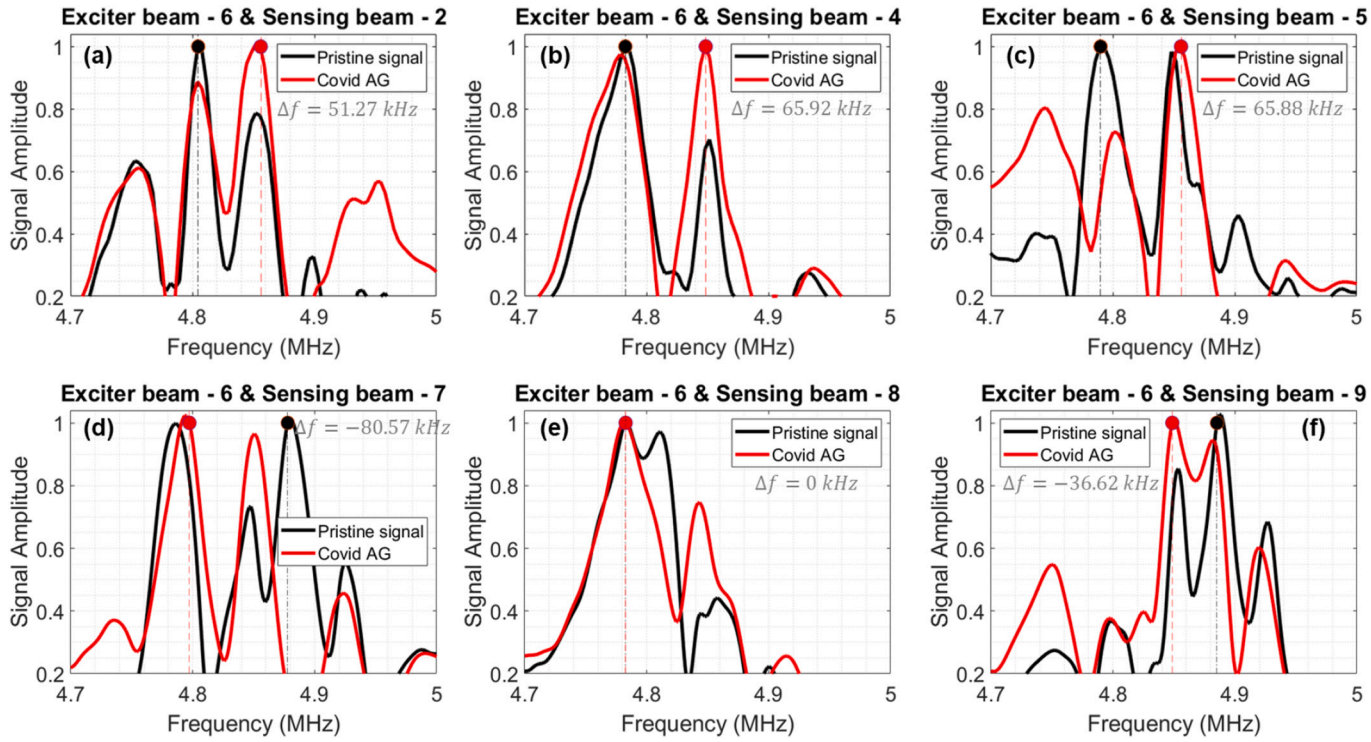

Fig. 8. Normalized FFT signal comparison of different beams and their frequency shifts between the pristine and the antigens baseline at 4.9 MHz.

(2.9 MHz and 4.9 MHz), results from 4.9 MHz are presented herein. Results and conclusions at both frequency ranges are similar and discussion on 2.9 MHz is omitted for brevity. Detailed spectral variations were investigated and compared for the pristine and antigen baseline configurations. Terminals 2,4 and 5 those are located on the left side of beam 6, resulted in a positive frequency shift of the peak frequency around the vicinity of 4.9 MHz. About 51.27 kHz, 65.92 kHz, and 65.88 kHz, respectively. Whereas the sensor beams on the right side of beam 6,

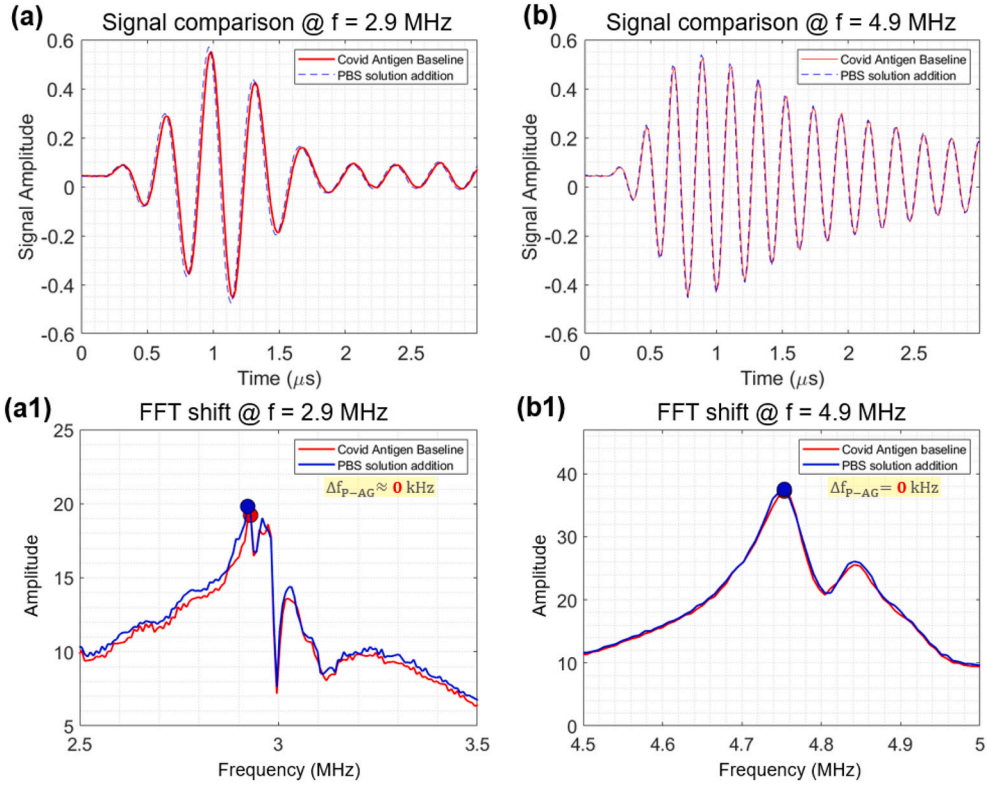

Fig. 9. Signal comparison between the antigens baseline and PBS solution at (a) 2.9 MHz and (b) 4.9 MHz. FFT of the signals comparison at (a1) 2.9 MHz and (b1) 4.9 MHz.

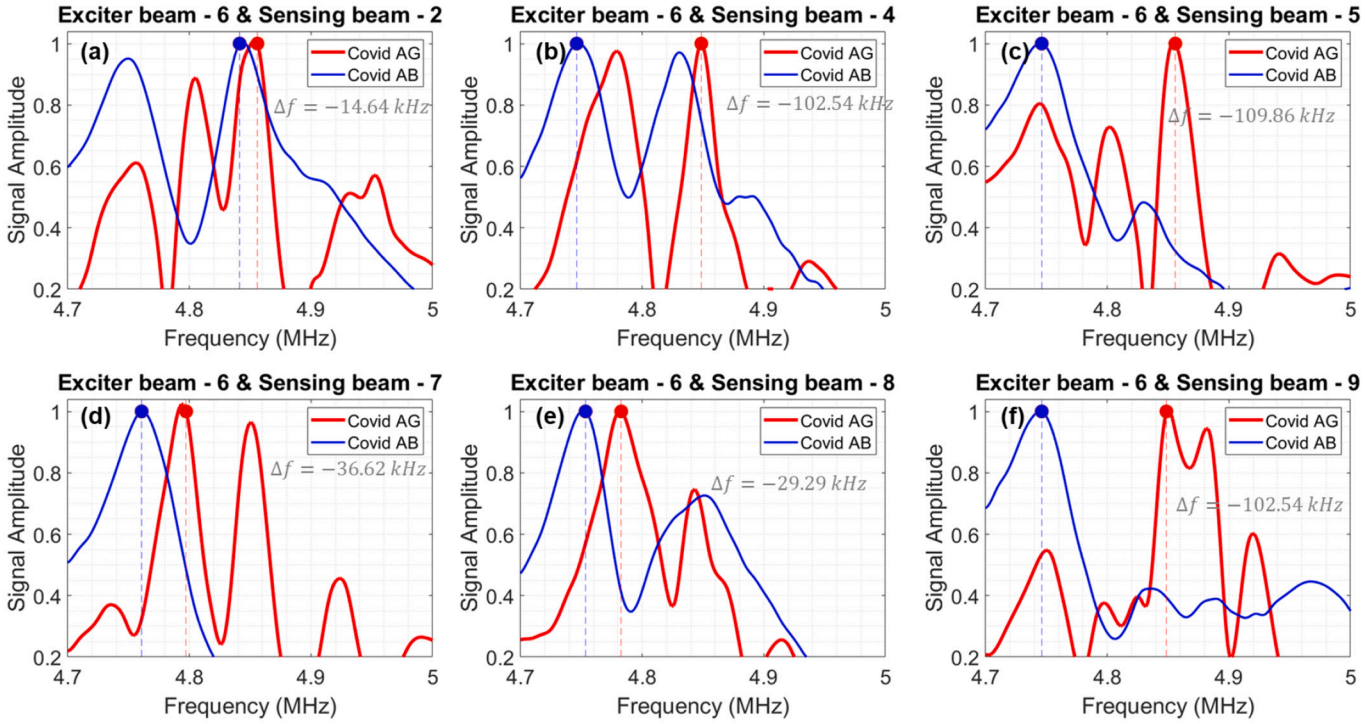

Fig. 10. Signal comparisons of pristine vs. antigens baseline vs. antibodies with exciter beam 6 and (a) sensing beam 8 and (b) sensing beam 4. FFT signal comparisons (a1) sensing beam 8 and (b1) sensing beam 4.

namely beam 7, 8, and 9 displayed a negative frequency shift of the peak frequency except terminal 8. Approximately −80.57 kHz, 0 kHz, and −36.62 kHz, respectively. It is evident that most of the beams demonstrated promising responses in the frequency domain with significant variation of their respective peak frequency content. Such shifts at the range of kHz are substantial in terms of sensitivity for micro/nano scalar detection. Fig. 8 shows the frequency spectrum of the acquired signals at a few sensing beams and their respective variations between the pristine and the antigens 'baseline' cases. Please note that terminal 8 has no frequency shift owning to symmetric wave mode in both the x and y directions discussed in Fig. 6d based on its unique geometrical shape and size. Symmetric wave mode in both directions creates ribs and pockets on the material surface which make it less sensitive to mass loading. This is evident from Fig. 8(e). However, if the mass loading exceeds its threshold, frequency shift will be evident and discussed later when the capture antibodies were added. This exact scenario infact enhances the selectivity of the detection.

4.4. Detection of SARS-COV-2 capture antibodies

In this section, the detection of COVID-19 capture antibodies is investigated and confirmed using additional signal analysis techniques. The detection of the antibodies using different acoustic signal analysis methods are discussed below.

4.4.1. Detection of SARS-COV-2 capture antibodies using FFT signal analysis

The sensor was first validated for selectivity at the beginning before the detection of the capture antibodies to check for cross-reactivity. The purpose of this step was to inspect if the sensor gets affected due to the non-target binding or the mass addition. An exact volume of the solvent (only PBS) was appended to the sensing platform (on top of antigens 'baseline'). The resulted signals with actuation frequencies 2.9 and 4.9 MHz were captured and analyzed for all the beams (but only sensor 8 is displayed in Fig. 9 because according to Fig. 8 the peak frequency shift in beam 8 was almost negligible). If the sensor beam is selective, it should not show any frequency shift. Fig. 9 shows both the time domain (Fig. 9 (a), 9(b)) and frequency domain (Fig. 9(a1), 9(b1)) ultrasonic signals acquired from terminal 8 after the addition of the PBS layer over the antigens 'baseline' sensing platform.

The sensing signals were captured before and after the addition of PBS solution and are superimposed at 2.9 and 4.9 MHz respectively (Fig. 9). The signal received after the addition of PBS layer depicts negligible changes in the time domain signals and almost no change (0 kHz shift) in the peak frequency response. Thus it proves the hypothesis of the selectivity with respect to the case of non-target binding responses due to the mass loading. To emphasize please note that the beam 8 has negligible shift when antigens were added and further PBS were added on top of the antigen 'baseline'. If this beam indicate any shift, when antibodies are added, will result a selective detection, concurring and cross verifying with other beams responses and thus enhance the sensitivity, simultaneously.

In the next segment, the capture antibodies were added and beam 6 was excited again. It was ensured that responses from the terminals were acquired at different frequencies. The FFT signals from most of the beams displayed positive frequency shifts upon the addition of the SARS-COV-2 capture antibodies including our focus beam 8. Although the SARS-COV-2 antibodies were placed on all the beams and signals were acquired from the terminals, for brevity, only a few results are presented herein. The FFT analysis of the sensor beam 2,4,5,7,8 and 9 are described in this section. Beam 8 exhibited the most fruitful results consistently. Fig. 10 shows a comparison between the signals acquired by the respective sensing beams, before and after the addition of the antibodies (*capture antibodies*). The waveforms in time domain signals (not shown) are clearly different for both the sensors before and after the addition of the capture antibodies, unlike when the PBS non-target binding solution was added. Next frequency domain analyses were performed to identify the shifts in the peak frequency amplitudes. It was clearly evident that after the addition of the COVID-19 antibodies, all signals at all the terminals made a negative frequency shift in most of the sensing beams compared to its antigens 'baseline'. Sensing beam 2, 4 and 5 exhibited frequency shifts of −14.64 kHz, −102.54 kHz and −

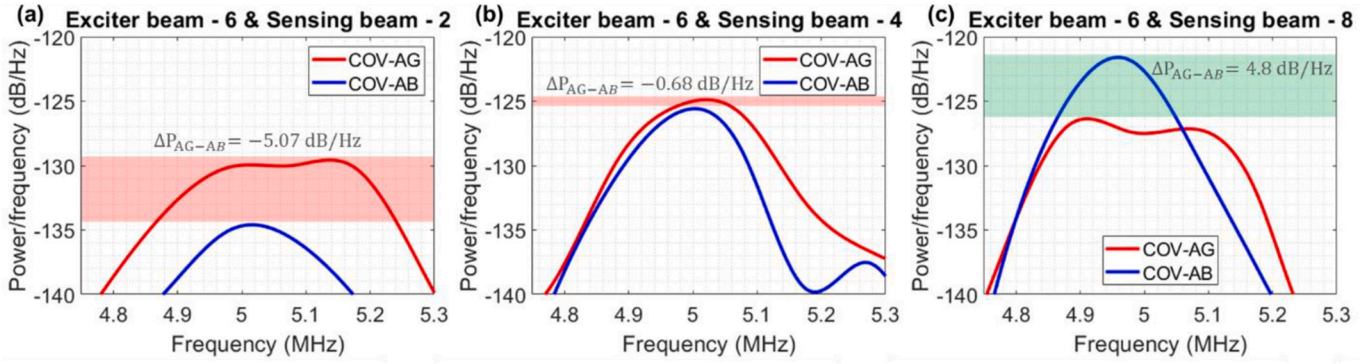

Fig. 11. Power Spectral Density (PSD) plots comparisons before and after the addition of COVID-19 antibodies of (a) Sensor 2, (b) Sensor 4 and (c) Sensor 8. Zoomed plot at 4.9 MHz of (a1) Sensor 2, (b1) Sensor 4 and (c1) Sensor 8.

109.86 kHz. Similarly, sensing beam 7, 8 and 9, displayed frequency shifts of −36.62 kHz, −29.29 kHz and − 102.54 kHz, respectively.

Sensing beam 5 was recorded as the highest shift approximately of −109.86 kHz, cross verifying each other (specifically with beam 8) towards the detection of SARS-COV-2 antibodies, serving the purpose of creating multi-geometry beams in the same sensor platform. The frequency shifts varied for different sensing beams at different excitation frequencies. Overall, it was clearly witnessed that most sensing beams showing an significant response to the addition of the antibodies. The detection were in kilohertz range (up to a couple of hundreds), that covers a wide spectrum for the frequency shift-based detection for the diagnosing purpose and thus, indicating to a highly sensitive sensing platform even to the slightest biophysical changes.

4.4.2. Additional feature extraction - power spectral density (PSD)

Here, additional features were extracted from the signals to prove the binding of antigen-antibody which validates the reliable functionality of sensors. Power Spectral Densities (PSD) were estimated from all the signals when beam 6 was used as an exciter. The PSD constitutes the total signal power contribution from each frequency component of a particular signal. PSD is a frequency response of any signal irrespective of periodic or random signal data and it signifies the average power distribution as a function of frequency. Here Welch's power spectral density estimation [27–29] was used. Fig. 11 shows the PSD of the signals collected before and after the addition of the antibodies from the terminals sensors 2,4 and 8, respectively.

From PSD analysis, near 4.9 MHz a trend was observed. It was seen that the amplitude of the power/frequency value in dB/Hz increased with the increasing length of the sensor beams when the COVID-19 antibodies were added to the sensor surface. For example, sensor 2 being one of the shorter beams, showed a power/frequency value of approximately −135 dB/Hz. Sensor 4 had a value of −128 dB/Hz. But the best response was exhibited by sensor 8 having an amplitude of −122 dB/Hz. Here, it is interesting to see that PSD for all the sensors with and without COVID-19 capture antibodies has a difference. These differences are higher and negative for the shorter beams but with a gradual reduction of the peak difference, larger beams have a positive difference. Irrespective of the changes all beams collectively and individually detected the presence of COVID-19 capture antibodies. Hence, the design of the biosensors was successful. In the future, an aggregate algorithm could be devised for easy detection of COVID- antigen-antibody combination by cross-verifying the results from all beams instrumented in the point of care biosensor. The authors intend to integrate the aggregated algorithm from all the data extracted from the sensing beams and transform it to a binary coded output stating 'positive' or 'negative' results only for the distinct commercialization process and for ease of operation in the next phase.

5. Conclusion

In this article, we have successfully demonstrated a lithium niobate piezoelectric cantilever-based lab-on-a-chip POC biosensor. The unique sensing method relies on the effective design of the piezoelectric cantilever beams of varying lengths made of lithium niobate crystal. Ultrasonic guided wave-based sensing using cantilever configuration was achieved. Conventional surface acoustic wave (SAW) sensors are used using the physics of Guided wave, however, multiple detection in a same platform is not possible and with desired sensitivity and selectivity through cross verification of the detection in single device. In this proposed method, Guided wave ultrasound is used but was exploited at multiple detection ports creating array of cantilever beams of varying lengths. Please note that here bending of the cantilever beams are not the physics used for detection, but the Guided wave propagated in each beam element at a modal frequency is used for the detection. Although the new platform is developed and intended for antigen diagnostic processes, it is equally effective for discovering new antibodies. The geometrically varying functionalized piezoelectric cantilever beams produce a wider spectrum of frequency response that contributes directly to detecting the slightest biophysical changes by cross verifying the detcec tion from the neighboring cantilever elements. Unlike the other conventional piezoelectric-based biosensor, owing to the wider frequency coverage, the proposed cantilever design and robust signal analyses have the leading edge in a reliable diagnostic process. In addition, the advanced technology of multiple signal feature extraction covers an ample opportunity in which different bio-samples, even to the slightest concentration have the ascended chances of captuting. Although not demonstrated, we hypothesize that using the proposed physics, detection using one or the other acoustic features escalate the sensitivity of the POC biosensor by many folds, all under a single platform. With limited resources, we have demonstrated the functionality and the proof of concept of the POC piezo-cantilever -based biosensor, however, reusability, detection limit quantification, ultra-miniaturization, integration with the microfluidic platform are work in progress. The developed piezoelectric-cantilever-based POC biosensor is not only limited to COVID-19 but many other bio-diagnostics and we strongly believe that this sensor will demonstrate rapid results for future disease outbreaks more reliably.

Declaration of Competing Interest

None.

Acknowledgments

The research was partially funded by the United States of Department of Agriculture (USDA) AFRI Grant No. 2017-67017-26167. The

effort was to create biosensor for detection of mycotoxin in samples collected from a corn field and to faciliate data for Toximap, however, during the pandemic the effort was branched out to find the possibility of effective detcetion of COVID-19 antibodies owing to the universal pysics of piezoelectric biosensor, as reported in this article.

References

[1] JHUoMCr center, 2020. https://coronavirus.jhu.edu/.
[2] Stanley A. Plotkin, Vaccines: past, present and future, Nat. Med. 11 (4) (2005) S5–S11.
[3] Shariq Suleman, Sudheesh K. Shukla, Nitesh Malhotra, Shikandar D. Bukkitgar, Nagaraj P. Shetti, Roberto Pilloton, Jagriti Narang, Yen Nee Tan, Tejraj M. Aminabhavi, Point of care detection of COVID-19: advancement in biosensing and diagnostic methods, Chem. Eng. J. 414 (2021) 128759.
[4] Shikandar D. Bukkitgar, Nagaraj P. Shetti, Tejraj M. Aminabhavi, Electrochemical investigations for COVID-19 detection-a comparison with other viral detection methods, Chem. Eng. J. 420 (2021), 127575.
[5] Neeraj Kumar, Nagaraj P. Shetti, Somanath Jagannath, Tejraj M. Aminabhavi, Electrochemical sensors for the detection of SARS-CoV-2 virus, Chem. Eng. J. 430 (2022), 132966.
[6] Nagaraj P. Shetti, Amit Mishra, Shikandar D. Bukkitgar, Soumen Basu, Jagriti Narang, Kakarla Raghava Reddy, Tejraj M. Aminabhavi, Conventional and nanotechnology-based sensing methods for SARS coronavirus (2019-nCoV), ACS Appl. Bio Mater. 4 (2) (2021) 1178–1190.
[7] S. Vigneshvar, C.C. Sudhakumari, Balasubramanian Senthilkumaran, Hridayesh Prakash, Recent advances in biosensor technology for potential applications–an overview, Front. Bioeng. Biotechnol. 4 (2016) 11.
[8] Saraju P. Mohanty, Elias Kougianos, Biosensors: a tutorial review, IEEE Potent. 25 (2) (2006) 35–40.
[9] Lo Gorton (Ed.), Biosensors and Modern Biospecific Analytical Techniques, Elsevier, 2005.
[10] Olivier Lazcka, F. Javier Del Campo, F. Xavier Munoz, Pathogen detection: a perspective of traditional methods and biosensors, Biosens. Bioelectron. 22 (7) (2007) 1205–1217.
[11] Guoguang Rong, Yuqiao Zheng, Yin Chen, Yanjun Zhang, Peixi Zhu, Mohamad Sawan, COVID-19 diagnostic methods and detection techniques: a review, Ref. Module Biomed. Sci. (B978-0-12-822548-6-7) (2021), https://doi.org/10.1016/B978-0-12-822548-6.00080-7.
[12] Elder A. de Vasconcelos, Newton G. Peres, Cintya O. Pereira, Valdinete L. da Silva, Eronides F. da Silva, Rosa F. Dutra, Potential of a simplified measurement scheme and device structure for a low cost label-free point-of-care capacitive biosensor, Biosens. Bioelectron. 25 (4) (2009) 870–876.
[13] J. Wang, Electrochemical biosensors: towards point-of-care cancer diagnostics, Biosens. Bioelectron. 21 (2006) 1887–1892.
[14] S.A. Soper, K. Brown, A. Ellington, B. Frazier, G. Garcia-Manero, V. Gau, et al., Point-of-care biosensor systems for cancer diagnostics/prognostics, Biosens. Bioelectron. 21 (2006) 1932–1942.
[15] V. Tsouti, C. Boutopoulos, I. Zergioti, S. Chatzandroulis, Capacitive microsystems for biological sensing, Biosens. Bioelectron. 27 (1) (2011) 1–11.
[16] X. Zhu, C.H. Ahn, Electrochemical determination of reversible redox species at interdigitated array micro/nanoelectrodes using charge injection method, IEEE Trans. Nanobiosci. 4 (2005) 164–169.
[17] Zhiwei Zou, Junhai Kai, Michael J. Rust, Jungyoup Han, Chong H. Ahn, Functionalized nano interdigitated electrodes arrays on polymer with integrated microfluidics for direct bio-affinity sensing using impedimetric measurement, Sensors Actuators A Phys. 136 (2) (2007) 518–526.
[18] Hannaneh Kabir, Mohsen Merati, Mohammad J. Abdekhodaie, Design of an effective piezoelectric microcantilever biosensor for rapid detection of COVID-19, J. Med. Eng. Technol. 45 (6) (2021) 423–433.
[19] Boli Zuo, Shanmao Li, Zhao Guo, Jinfang Zhang, Chuanzhi Chen, Piezoelectric immunosensor for SARS-associated coronavirus in sputum, Anal. Chem. 76 (13) (2004) 3536–3540.
[20] Hyung Hoon Kim, Hyeong Jin Jeon, Hyun Kook Cho, Jea Hun Cheong, Hyeong Soon Moon, Jeung Sang Go, Highly sensitive microcantilever biosensors with enhanced sensitivity for detection of human papilloma virus infection, Sensors Actuators B Chem. 221 (2015) 1372–1383.
[21] Kyung Wook Wee, Ghi Yuun Kang, Jaebum Park, Ji Yoon Kang, Dae Sung Yoon, Jung Ho Park, Tae Song Kim, Novel electrical detection of label-free disease marker proteins using piezoresistive self-sensing micro-cantilevers, Biosens. Bioelectron. 20 (10) (2005) 1932–1938.
[22] Fumio Narita, Zhenjin Wang, Hiroki Kurita, Yu Zhen Li, Shi Jia Yu, Constantinos Soutis, A review of piezoelectric and magnetostrictive biosensor materials for detection of COVID-19 and other viruses, Adv. Mater. 33 (1) (2021) 2005448.
[23] Riccarda Antiochia, Developments in biosensors for CoV detection and future trends, Biosens. Bioelectron. 173 (2021), 112777.
[24] Thangavel Lakshmipriya, Uda Hashim, Subash C.B. Gopinath, N. Azizah, Microfluidic-based biosensor: signal enhancement by gold nanoparticle, Microsyst. Technol. 22 (10) (2016) 2389–2395.
[25] Suchera Loyprasert, Panote Thavarungkul, Punnee Asawatreratanakul, Booncharoen Wongkittisuksa, Chusak Limsakul, Proespichaya Kanatharana, Label-free capacitive immunosensor for microcystin-LR using self-assembled thiourea monolayer incorporated with ag nanoparticles on gold electrode, Biosens. Bioelectron. 24 (1) (2008) 78–86.
[26] José M. Pingarrón, Paloma Yanez-Sedeno, Araceli González-Cortés, Gold nanoparticle-based electrochemical biosensors, Electrochim. Acta 53 (19) (2008) 5848–5866.
[27] Sukhada A. Unde, Revati Shriram, Coherence analysis of EEG signal using power spectral density, in: 2014 Fourth International Conference on Communication Systems and Network Technologies, IEEE, 2014, pp. 871–874.
[28] Solomon Jr, M. Otis, PSD Computations Using Welch's Method. [Power Spectral Density (PSD)]. No. SAND-91-1533, Sandia National Labs, Albuquerque, NM (United States), 1991.
[29] P.K. Rahi, R. Mehra, Analysis of power spectrum estimation using welch method for various window techniques, Int. J. Emerg. Technol. Eng. 2 (6) (2014) 106–109.